**DAS microseismic monitoring results from the July 2023 circulation tests at the Utah FORGE geothermal underground laboratory**

*Ismael Vera Rodriguez*, Joseph Wolpert, David Podrasky, Thomas Coleman, Carlos Maldaner, Silixa, Yuanyuan Ma, Michal Chamarczuk, Jonathan Ajo-Franklin, Rice University, and Matt Becker, California State University Long Beach*

# DAS microseismic monitoring at Utah FORGE


## SUMMARY

We analyzed distributed acoustic sensing (DAS) data recorded in two wells during circulation tests performed on July 2023 at the Utah FORGE geothermal underground laboratory. We applied hierarchical clustering to detected microseismicity to aid in the selection of a subset of events that were used to jointly invert for their location and a new 1D velocity model for the site. Another subset of carefully selected events was then located with the new velocity model and used as references to estimate the relative locations of the rest of the catalogue of 257 event detections. The locations describe three fracture planes mapped asymmetrically and perpendicular to the direction of the injection well. Moment magnitudes estimated independently from P- and S-waves using new formulations in distributed strain agree on a crossplot and correlate well with estimations derived from gephone data. The new velocity model will be used to estimate event locations in ongoing baseline microseismic monitoring in the site and also in upcoming planned stimulations. The estimated locations show visibly higher resolution compared to previously reported results using a surface geophone network and potentially change the interpretation derived from those results.


## INTRODUCTION

The Frontier Observatory for Research in Geothermal Energy (FORGE) is an underground laboratory sponsored by the US Department of Energy. The laboratory, located in Utah over the flank of a granitic intrusion (Allis et al., 2018), is a test bed that institutions use for advancing research in enhanced geothermal systems.

The purpose of the July 2023 circulation tests was to investigate hydraulic connection between wells 16A(78)-32 and 16B(78)-32, acting as injection and production wells, respectively. The injection well was hydraulically fractured in three stages a year before in April 2022. Two of these stages occurred through perforated casing and one in open hole. During the circulation tests considered in this study, the injection rate was maintained low on purpose to prevent additional hydraulic fracturing. A more detailed overview of these tests is presented in Niemz et al. (2024).

The circulation tests happening on July 19 and 20 were monitored using DAS cables deployed on the production well and the additional monitoring well 78B-32 (Figure 1a). A multimode fiber in well 16B was interrogated with a Silixa iDAS™ v3 unit at a sampling rate of 0.1 ms using a gauge length of 10 m. The total number of channels recorded in this well was 3,264 at spacings of approximately 1 m. As a result of manufacturing difficulties with the cable, a higher than usual noise floor was observed in this well. A singlemode fiber in well 78B was interrogated using a Silixa iDAS v2 system with the same gauge length and approximate channel spacing as in well 16B, albeit with a lower sampling rate of 1 ms. The total number of channels in this well was 1,344. In both cases, the fibers were cemented behind the casing.

The injection in well 16A started at about 18:00 p.m. UTC time on July 18. Figure 1b shows the rate of microseismic events detected until the end of this circulation test on July 20. In total there were 257 event detections, although some of them correspond to more than one closely spaced events detected within the same time window. In the remaining of this work, we describe the processing performed to this dataset for the estimation of a 1D velocity model for the site and the location and magnitude of the detected microseismicity.

## METHODS

### Hierarchical clustering

First, the crosscorrelation matrix between all events was sorted using hierarchical clustering (Gordon, 1987). The objective was to identify potential clusters of similar microseismic events and select samples from each cluster to run a joint location and velocity model inversion (Figure 2).

### Joint event location and velocity model inversion

Using five microseismic events from different apparent clusters, an optimization algorithm based on particle swarm optimization (Vera Rodriguez, 2019) was implemented to jointly estimate a 1D velocity model and the event locations. The estimated model parameters included velocities for P- and S-waves and the layers depths. The number of model layers was preset by looking at apparent velocity changes in wave arrivals on the DAS data. The input to the optimization were time picks set over the observations of direct P- and S-arrivals of the microseismic events. The apex of the arrivals was nearly captured in some of the data examples of well 16B. As this information is particularly helpful to constrain the event location the density of picks near this region was increased with respect to the rest of the DAS channel ranges (see Figure 3c for an example).

### Selection of reference events

In a first run of the workflow, the absolute locations of the events used to estimate the 1D velocity model were refined individually. The absolute location method consisted in fitting the arrival time picks of direct P- and S-waves. These events were then used as references to locate the rest of the catalogue of microseismic event detections. After a first run of relative location, a new subset of

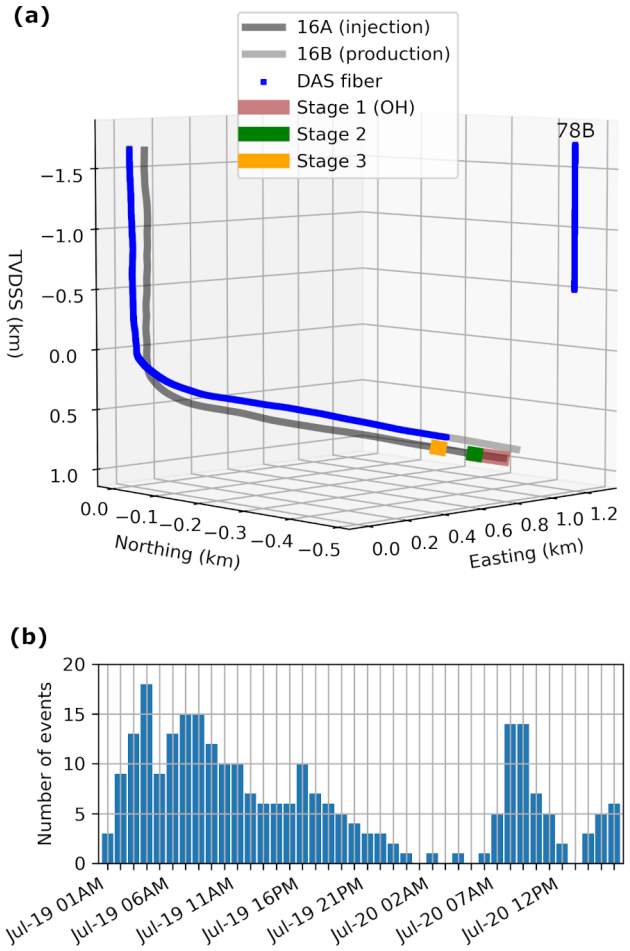


Figure 1: (a) Well geometries and location of the monitoring DAS cables. (b) Time distribution of events detected during the circulation test in this study. Times are UTC.

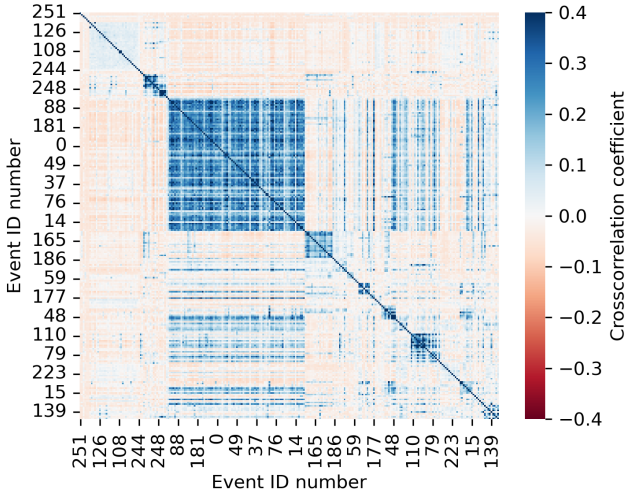


Figure 2: Crosscorrelation matrix for the catalogue of detected microseismic events after hierarchical clustering.

reference events was chosen, this time using as main selection criterion their spatial distribution over the full apparent shape of the microseismic cloud. This final set of reference events consisted of nine elements for which absolute locations were also estimated.

**Relative locations**

The relative location method consisted in calculating grids of differential travel times for direct P- and S-arrivals in the neighborhood of each reference event (Zhang and Wen, 2015). During the relative location process, the target event was crosscorrelated with each of the reference events. The correlation gather that produced the largest crosscorrelation coefficient was then selected to produce stacked traces for P- and S-waves at each of the nodes of the local grid of the corresponding reference event. The stacked traces were produced by correcting the correlation gathers by the differential travel times before stacking them; afterwards, the peak of the weighted sum of P and S stacked traces was assigned to the corresponding grid node. Details of the implementation used in this study can be found in Shashidar et al. (2020).

For the evaluation of the quality of individual results, the theoretical arrival times forward modelled using the estimated relative location were used as reference to extract wave arrivals and estimate mean signal-to-noise ratios (SNR) for P- and S-waves among all DAS channels. These values together with SNR standard deviations, distance between reference and target event, correlation coefficient between reference and target event, and peak amplitude in the relative location grid were combined in an empirical formula to generate a Confidence Index (CI) that could be used to filter the best location results for further analysis.

**Magnitudes**

Magnitudes were estimated by following the derivation of the classical moment magnitude formulas (Aki and Richards, 2009) but in terms of distributed strain. This also required the calculation of new spherical averages for pure double couple sources in terms of distributed strain units. The averages were estimated numerically and used with the new derived formulas together with the DAS data in its native distributed strain units.

As described above, theoretical arrival times for P- and S-waves could be used as reference to extract direct arrivals for the calculations. In this case, only wave arrivals with SNR $> 4$ were considered in the processing. Additional to the mean and standard deviation of the SNR of wave arrivals, the total vertical aperture subtended by the considered DAS channels was calculated to help in qualifying the confidence in a $M_w$ result. Independent estimations were generated from P- and S-waves that were then combined with a mean to obtain a final $M_w$ for any given event. Assuming perfect cable coupling, the derived formulas provide true $M_w$ estimations. Without site specific calibration these results are considered relative estimates.

## RESULTS

The swarm evolution for both event locations and velocity model parameters shows additional combinations of the inverted variables that produce a good fit to the observations (dark gray areas in Figure 3a and b). These are local minima that were explored by the swarm before arriving to the final solution. The optimization was reinitialized five times from different random swarm states and the final solution with the lowest cost was chosen to fix the velocity model for the processing of the microseismic data (Figure 3a). This velocity model consists of eight layers with thicknesses varying from $\sim$ 130 m to about 580 m. On the other hand, $V_p/V_s$ ratios range in the interval from $\sim$1.63 to $\sim$2.2 Shallower layers present the higher $V_p/V_s$ ratios, i.e., consistent with previous observations for sedimentary layers with lower compaction (Chung et al., 1990).

After a first run of relative location using as reference events the set that was input to the joint location and velocity model inversion, the arrangement of the microseismic cloud into three planes was already visible to some extent; thus, a final set of nine reference events could be chosen at strategic locations covering the main extent of the microseismic cloud. With this set of reference events, the definition of the three planes outlined by the microseismicity improved after a second run of relative location (Figure 4). Uncertainty ellipsoids derived from the relative location probability volumes display a mean extent of $\sim$32 m on their longest axis, and $\sim$13 m on their shortest axis. The shortest axis was normally (quasi)vertically orientated (Figure 4b and c). The asymmetry with respect to 16B may be partly the result of detection bias, where events north of 16B could not be detected on 78B to constrain their position without the location ambiguity inherent to the cable geometry in 16B alone.

The vertical coordinates of the located microseismicity are mostly contained within the depth range of 570 m to 750 m from mean sea level. As the extent of the located microseismicity does not reach the injection well 16A, it is difficult to correlate the planes outlined by the microseismic cloud with the hydraulic fractures previously created in well 16A. Nevertheless, the DAS results represent a significant improvement in resolution when compared to previous results obtained using surface and shallow borehole geophones (Niemz et al., 2024), where the locations do not permit the discrimination of multiple fracture planes (Figure 4b and c). Compared to microseismic activity observed during stimulation of stages 1 through 3 in well 16A a year before, the inclination of the planes outlined by the DAS results appear to extrapolate closer to the microseismicity observed during stage 3 (Figure 4c).

Magnitudes estimated independently from P- and S-waves agree close to a 45° line on a crossplot (Figure 5a), although P-wave results are in some cases slightly higher. This could be an effect of the spherical average approximation for the source radiation pattern but the effect of amplitude corrections for anelastic attenuation cannot be discarded. As we did not have information

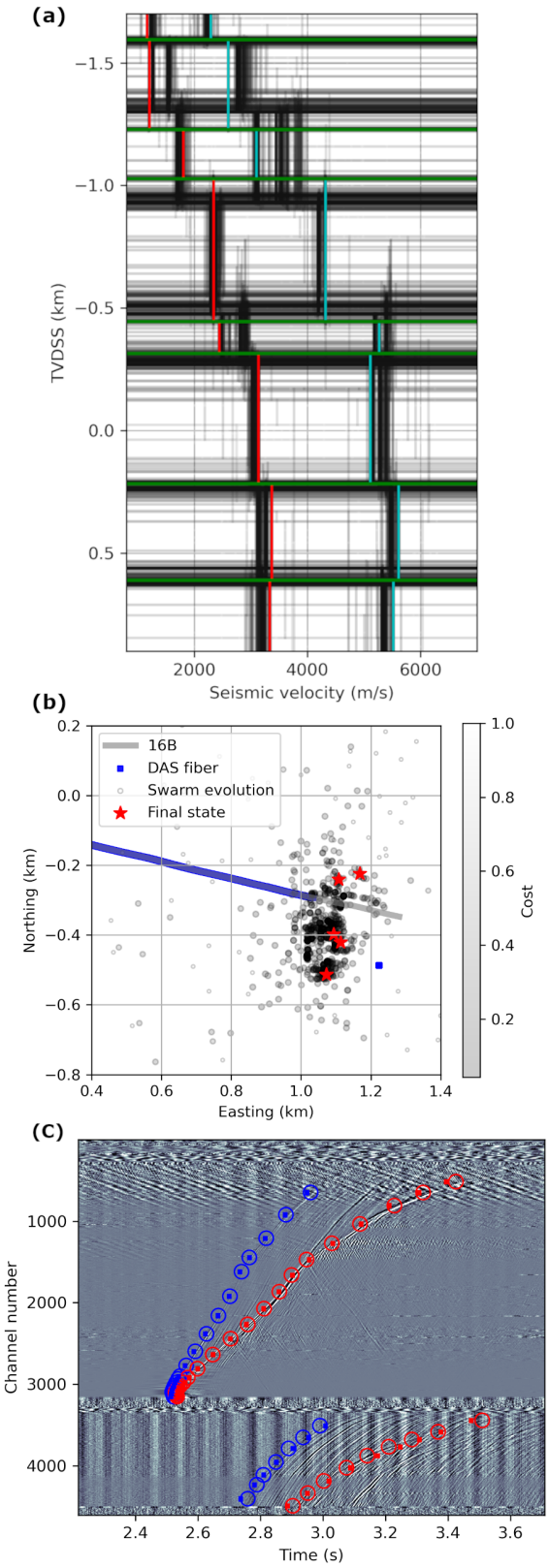


Figure 3: Swarm state (gray colors) during joint optimization for event locations and velocity model. (a) Model layer depths and seismic velocities. Green lines show the final state for layer interfaces, and cyan and red lines the final state for P- and S-wave velocities, respectively. (b) Map view of the swarm evolution for event locations. (c) Example of fit between manual time picks (circles) and theoretical arrival times (dots) forward modelled with the selected final solution.

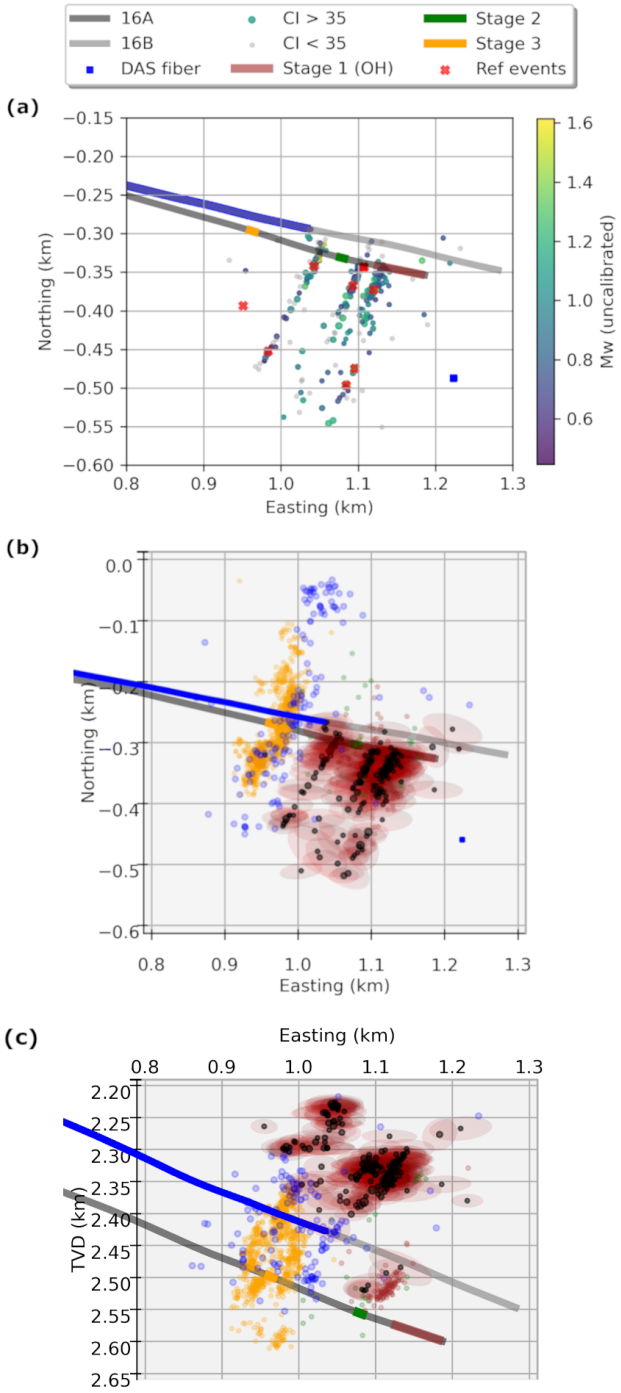


Figure 4: (a) Map view of relative location results. Events are filtered by confidence index (CI) and colored by their estimated magnitude (uncalibrated). (b) Map view and (c) side view of uncertainty ellipsoids for events with CI>35. The panels also display event locations from the 2022 stimulations (Dyer et al., 2023) colored by their corresponding stage, and in blue the locations estimated with the surface network for circulation events detected during the same time period of the DAS records (Niemz et al., 2024).

available regarding $Q_p$ and $Q_s$, values of 200 were used for both wave types. Given the relatively short distances between the microseismic sources and the DAS channels, these values did not produce significant amplitude corrections.

The uncalibrated DAS magnitudes fall mainly within the approximate range of $M_w$0.5 to $M_w$1.3, this is about 1.15 orders of magnitude larger than what was estimated using shallow borehole geophone data (Niemz et al., 2024). Using Niemz et al. (2024) results to calibrate our DAS magnitudes produces a good match around a 45° line on a crossplot (Figure 5b), reducing also their approximate range to between $M_w$-0.6 and $M_w$0.2. The range of magnitudes covered by the distribution is too short to apply the maximum likelihood method, nevertheless, it is possible to fit manually the distribution with a b-value $\sim$ 1.8.

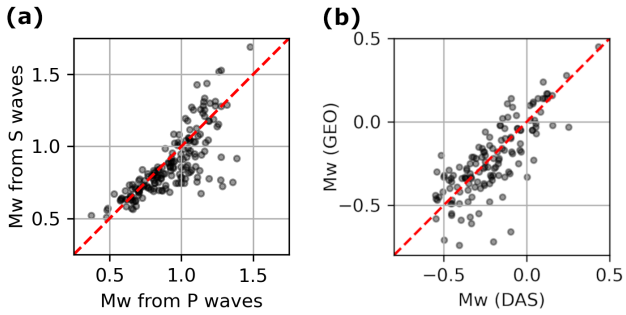


Figure 5: (a) Comparison of independent and uncalibrated $M_w$ estimations from P- and S-waves in distributed strain. (b) Crossplot of calibrated $M_w$ estimated with DAS and $M_w$ reported by Niemz et al. (2024). Red dashed lines have a 45° slope.

## CONCLUSIONS

Circulation tests were conducted at Utah FORGE during July 2023 to assess the connectivity between wells 16A and 16B. The tests were monitored with different technologies including DAS with two fiber optic cables interrogated independently and located on different wells. A total of 257 detections were verified, but the number of visible events is higher as several detections showed more than one closely spaced microseismic events within the same detection window. Clusters of similar events could be identified after sorting the crosscorrelation matrix of the catalogue of events, nevertheless, the clusters may not be very dissimilar given their relatively close spatial distribution. A subset of microseismic events could be used to estimate a new 1D velocity model for the site jointly with their source locations. Using the new velocity model and another subset of carefully selected reference events it was also possible to estimate relative locations for the rest of the microseismicity catalogue. The microseismic cloud describes three fracture planes. As the detected cloud does not illuminate the planes down to the trajectory of well 16A it is not straightforward to interpret if these planes correspond with hydraulic fractures previously created in this well. The magnitudes of the microseismic catalogue after calibration using results derived from geophone data fall mostly within the range from $M_w$-0.6 to $M_w$0.2

## ACKNOWLEDGMENTS

Work carried out for research at the Utah Frontier Observatory for Research in Geothermal Energy (FORGE) was funded in part by the US Department of Energy, under DE-EE0007080.

## REFERENCES

Aki, K., and P. Richards, 2009, Quantitative seismology: University Science Books.

Allis, R., M. Gwynn, C. Hardwick, W. Hurlbut, and J. Moore, 2018, Thermal characteristics of the FORGE site, Milford, Utah: Geothermal Resources Council Transactions, **42**, 1011–1025.

Chung, T., N. Hirata, and R. Sato, 1990, Two-dimensional P- and S-wave velocity structure of the yamato basin, the southern Japan sea from refraction data collected by an ocean bottom seismograph array: J. Phys. Earth, **38**, 99–147.

Dyer, B., D. Karvounis, and F. Bethmann, 2023, Microseismic event catalogues fom the well 16A(78)-32 stimulation in April, 2022 in Utah FORGE: http://dx.doi.org/10.31905/52CC4QZB.

Gordon, A., 1987, A review of hierarchical classification: J. R. Statist. Soc. A, **150**, 119–137.

Niemz, P., J. McLennan, K. Pankow, J. Rutledge, and K. England, 2024, Circulation experiments at Utah FORGE: Near-surface seismic monitoring reveals fracture growth after shut-in: Geothermics, 102947.

Shashidar, D., I. Vera Rodriguez, K. Mallika, D. Kühn, M. Wilks, H. Satyanarayana, and V. Oye, 2020, Relative locations of an earthquake sequence recorded during June 2017 on the Koyna–Warna borehole seismic network of western India: Bulletin of the Seismological Society of America, **110**, 3130–3138.

Vera Rodriguez, I., 2019, A heuristic-learning optimizer for elastodynamic waveform inversion in passive seismics: IEEE Transactions on Geoscience and Remote Sensing, **57**, 2234–2248.

Zhang, M., and L. Wen, 2015, An effective method for small event detection: match and locate (M&L): Geophysical Journal International, **200**, 1523–1537.